Image Processing Based Atmospheric River Tracking Method Version 1 (IPART-1)

Guangzhi XU[1], Xiaohui MA[1,3], Ping CHANG[2,3], and Lin Wang[4]

[1]Key Laboratory of Physical Oceanography, Institute for Advanced Ocean Studies, Ocean University of China and Qingdao National Laboratory for Marine Science and Technology, Qingdao, China

[2]Department of Oceanography and Department of Atmospheric Sciences, Texas A&M University, College Station, Texas, USA

[3]The International Laboratory for High-Resolution Earth System Prediction, Texas A&M University, College Station, Texas, USA

[4]Center for Monsoon System Research, Institute of Atmospheric Physics, Chinese Academy of Sciences, Beijing, China

Correspondence: Guangzhi XU (xugzhi1987@gmail.com)

Abstract. Automated detection of atmospheric rivers (ARs) has been heavily relying on magnitude thresholding on either the integrated water vapor (IWV) or integrated vapor transport (IVT). Magnitude thresholding approaches can become problematic when detecting ARs in a warming climate, because of the increasing atmospheric moisture. A new AR detection method derived from an image processing algorithm is proposed in this work. Different from conventional thresholding methods, the new algorithm applies threshold to the spatio-temporal scale of ARs to achieve the detection, thus making it magnitude independent and applicable to both IWV- and IVT-based AR detections. Compared with conventional thresholding methods, it displays lower sensitivity to parameters and a greater tolerance to a wider range of water vapor flux intensities. A new method of tracking ARs is also proposed, based on a new AR axis identification method, and a modified Hausdorff distance that gives a measure of the geographical distances of AR axes pairs.

1 Introduction

Many previous studies have demonstrated the dual hydrological roles played by atmospheric rivers (ARs), both as a fresh water source for certain water-stressed areas Dettinger (2011, 2013); Rutz and Steenburgh (2012) and a potential trigger for floods Lavers et al. (2012); Lavers and Villarini (2013); Neiman et al. (2008); Moore et al. (2012). Increasing attentions on ARs are seen not only among the research community, but also within water resource management agencies, risk mitigation managers and policy makers Ralph et al. (2019). Some of the pressing research questions that challenge the research community are: how ARs will respond to global warming? And how changes in ARs will affect future hydroclimate projections? Answers to these questions will require a set of robust AR detection methods that consider the nonstationary nature of the atmospheric responses to global warming.

The increased attention to AR research has led to the development of an array of AR detection and/or tracking methods with considerable variability in their design, complicity and targeted scientific questions. The Atmospheric River Tracking Method Intercomparison Project (ARTMIP) Ralph et al. (2018); Shields et al. (2018) was initiated as a community effort to systematically estimate the methodological uncertainties in AR detections. In the 1-month "proof-of-concept" analysis Shields et al. (2018), 15 different detection methods were included to quantify various AR-related statistics from the North America and Europe landfalling ARs. And the early start comparison work Ralph et al. (2018) included 8 methods, some of which also came with sub-catalogues with different parameter choices. All of these AR detection methods are based on either integrated water vapor (IWV), or integrate vapor transport (IVT), or a combination of both. For most of the algorithms compiled by ARTMIP, a pre-determined value is used as the magnitude threshold for the initial selection before subsequent geometrical considerations. For instance, (Ralph et al., 2004; Neiman et al., 2008; Hagos et al., 2015; Dettinger, 2011) identified ARs as contiguous regions where $IWV \geq 20\,mm$, at least $2000\,km$ in length and no more than $1000\,km$ in width. A $250\,kg/m/s$ IVT threshold was used by (Rutz et al., 2014, 2015) in detecting landfalling ARs onto the North America continent. These AR magnitude-thresholding methods have the advantage of being easy to use and straightforward to interpret.

An implicit assumption with this magnitude thresholding approach is that the atmospheric moisture level stays unchanged throughout the analysis period, or the temporal power spectrum remains constant across decadal or beyond timescales. As the threshold value used in the analysis is based on the historical observations, a question arises: whether the constant threshold value can be reliably used for AR detection under future warming climate as the atmospheric moisture level is expected to increase?

An alternative to the absolute magnitude threshold is the use of a chosen percentile of IVT or IWV at a given location as a threshold, such as a 85th percentile of local climatology used in some studies (e.g. (Lavers et al., 2012; Nayak et al., 2014; Guan and Waliser, 2015)). Such an approach grants the IVT or IWV threshold the sensitivity to the possible basin, seasonal or latitudinal differences. However, a prescribed percentile value may not have the flexibility to adopt to the fast-changing synoptic conditions where ARs are embedded. Furthermore, an additional 100 kg/m/s constant IVT threshold was found to be necessary to complement detections in the polar regions Guan and Waliser (2015).

Another disadvantage of the above approaches is the need for different thresholds for IWV-based and IVT-based applications, and in both cases, possibly different sets of thresholds for mid-latitude systems and polar systems. As demonstrated in (Gorodetskaya et al., 2014), lower air temperature and the reduced water holding capacity demand a separate set of threshold catered to the polar climate.

A possible solution to the problems is to avoid the usage of magnitude threshold, and instead apply the filtering process to moisture filament structures. Instead of thresholding the IVT or IWV magnitudes which show greater sensitivity to a cut-off value, we propose a method that performs the filtering on the spatio-temporal "spikiness" of IVT or IWV fields which are found to have lower sensitivity to parameter choices. This reduced parameter sensitivity makes it less prone to the problem of the nonstationary nature of the atmospheric moisture level under the warming climate.

A reasonable AR axis definition is a necessary prerequisite to accurate AR length estimate and a useful metrics for subsequent tracking. The accuracy of axis estimation has not received enough attention in literature, although sensitivities in

55 geometrical constraints have been highlighted Ralph et al. (2018). The AR axis is typically defined as a simple curve that follows the orientation of the AR, providing a summary of its geographical location and extent. (Wick et al., 2013) used the image processing algorithm skeletonization to find AR axes. This method has the advantage of being able to handle complex shapes and the resultant axis never goes out of the AR boundary. However, it lacks physical correspondences and the identified axes do not always follow the maximum intensities of the ARs.

60 Another method to identify the AR axis is to perform a curve fitting on the coordinates of the AR region. For instance, (Mundhenk et al., 2016) fitted a 3rd degree polynomial to the latitudes and longitudes of AR coordinates. For simple shapes this gives a satisfactory result, but for complex, curvy shapes, polynomial fitting suffers from the inability to handle multiple outputs (e.g. one longitude corresponds to more than one latitudes), and difficulties in finding a balance between over-fitting and under-fitting.

65 (Guan and Waliser, 2015) defined the AR axis by performing a perpendicular line-scan along the great circle between the furthest apart pair of AR region coordinates, and assigning axis points to the largest IVT value along the scanning line. For complex shapes the identified axis is not guaranteed to be a continuous curve.

Along with the new AR detection algorithm, we propose a new method to identify AR axis. By building a topological graph from AR region coordinates and the horizontal moisture flux vectors, the axis finding problem is transformed into a
70 path searching problem. With moisture flux information encoded into the formulation, the found AR axis has close physical correspondences, follows the major orientation of the flows, stays close to the maximum flux values, and never extends out of AR boundary. It is also capable of handling very complex shapes.

Many previous studies performing AR detection are solely concerned with determining AR presence at any given time/location. Only a few recent studies (e.g., (Sellars et al., 2017; Zhou et al., 2018; Guan and Waliser, 2019)) attempted to track ARs as
75 unique entities through their life cycle. In contrast, the trackings of tropical cyclones and extra-tropical storms have been a common practice. This is largely because the circular symmetry in these systems permits their locations being represented by a single coordinate pair, and inter-center vicinity being measured by either the distance between coordinate pairs (e.g. (Camargo and Zebiak, 2002; Murakami et al., 2015)), or an areal overlap ratio with the help of radii estimates (e.g. (Kew et al., 2010)). The complex shapes of ARs and the absent of circular symmetry deny such a convenience. In this work we also propose an AR
80 tracking algorithm in which a modified Hausdorff distance, which gives an effective measure of the geographical proximity of two ARs, is used as inter-AR distance estimate.

This work is mostly focused on the description and introduction of the new detection and tracking methods, using the application on North Hemisphere IVT data as an illustration. A more detailed comparison between ARs detected by this new method and other conventional methods are reported in a separate study. This paper is organized as follows: Section 2 gives
85 a description of the methods. Section 3 examines the parameter sensitives of the proposed method by comparing the AR detection results against those by two conventional detection methods. This is followed by an analysis of the the trackings of ARs in Section 4, and an illustration of applying the proposed method on IWV-based detections in Section 5. Lastly, Section 6 summarizes the results and discusses some limitations of these methods.

2 An Image Processing Based AR Detection and Tracking Method

2.1 AR detection using the top-hat by reconstruction (THR) algorithm

90

The AR detection method is inspired by the image processing technique *top-hat by reconstruction* (THR) Vincent (1993), which consists of subtracting from the original image a *greyscale reconstruction by dilation* image. In the context of AR detection, the greyscale image in question is the non-negative IVT distribution. The THR process starts by defining a "marker" image, which in this case is obtained by applying a greyscale erosion on the IVT data. Greyscale erosion (also known as minimum filtering,

95 e.g. (Dougherty, 1992)) can be understood by analogy with a moving average. Instead of the average within a neighborhood, erosion replaces the central value with the neighborhood minimum. Similarly, dilation replaces with the maximum. And the neighborhood is defined by the structuring element E, which is an important parameter in the entire THR process.

Then from the "marker" image lateral spread (dilation) starts. The dilation is capped in pixel intensity by the original IVT distribution, giving the greyscale reconstruction by dilation component (hereafter reconstruction), which corresponds to the

100 background IVT component. Finally, the difference between IVT and the reconstruction gives the anomalous IVT, from which AR candidates are searched. Intuitively, the THR algorithm consists of a search for a "baseline" intensity level within a given neighborhood (the erosion process), a creation of plateaus at this level (reconstruction), and a final segmentation of baseline and anomalies. Non-zero regions in this anomaly component are then selected, giving a collection of marked out regions in the data domain denoting the boundaries of potential ARs. More details of the THR algorithm are given in the Appendix, and

105 Fig. 1 gives some illustrations of this filtering process applied on 1D and 2D data.

The top panel of Fig. 1 shows a snapshot of the IVT field at an arbitrary time point, and a horizontal line denotes the position of a zonal cross-section, whose profile is shown in Fig. 1b. The blue curve in Fig. 1b shows the two prominent peaks with IVT values above $1000\,kg/m/s$. The green dashed curve shows the result of 1D erosion applied on this cross-section, where the structuring element E used is a line segment with length 13: $E = \underbrace{[1,\cdots,1]}_{13}$.

110 The result of the 1D erosion is used as the "marker" image, from which lateral spread (dilation) starts. The dilation is capped by the original IVT profile, giving the reconstruction plotted as dashed red curve. Finally, the difference between IVT and the reconstruction is defined as the anomalous IVT, plotted as the dashed black curve. The lateral extent of these horizontal plateaus across the local peaks is, by design, 13 pixels wide. Given that the data used in this case have a horizontal resolution of $0.75°$, this is equivalent to $\sim 1040\,km$, which is also the upper bound of typical AR width (see later sections).

115 However, this is too strict a cut that the prominent Atlantic AR is largely gone in the filtered curve. This is because this AR is well zonally oriented so that only the very tip of the IVT profile can fit into this zonal lateral extent. While the other AR in Pacific has a much narrower zonal extent therefore a larger portion of its peak is retained. For shallower peaks like the one around $170°E$, the filtering still gives a non-zero anomaly, but with a much smaller magnitude, properly reflecting their shallowness.

120 To address the missing Atlantic AR, the erosion and reconstruction processes are extended into 2D (x- and y- dimensions), using a 2D disk-like structuring element (a 2D mesh satisfying $\sqrt{x^2 + y^2} \le 6\,pixels$, 6 being chosen as it gives a diameter of

13 after adding a central pixel). The profiles of the results are plotted as solid curves in Fig. 1b. This time, about half the two prominent IVT peaks are attributed to the reconstruction component, and the other half to anomalies. The shallow peaks stay about the same.

125   Fig. 1c and d show the maps of 2D reconstruction and anomalies, respectively. Again, plateaus are created in the reconstruction field, above which are the anomalies. Exactly where in height a peak is cut depends on how wide the peak's shape is, and it is the direction with the greatest gradient that matters. For AR-like features, this corresponds to the cross-sectional direction along which the 6 pixel radius takes effect. This allows us to properly isolate plumes that are narrow in one direction but elongated in the other. Shallow peaks can also be retained, largely regardless of their smaller absolute magnitudes, as long

130 as the peaks stand out at the given spatial extent.

    We then extend the processes of erosion and reconstruction to 3D (i.e. time, x- and y- dimensions), measuring "spatio-temporal spikiness". The added temporal dimension helps detect plumes that are transient at a given temporal extent. The structuring element used for 3D erosion is a 3D ellipsoid:

$$E = \left\{ (z, x, y) \in \mathbb{Z}^3 \mid (z/t)^2 + (x/s)^2 + (y/s)^2 \leq 1 \right\} \tag{1}$$

135 with the axis length along the time dimension being t, and the axes for the x- and y- dimensions sharing the same length s. Both t and s are measured in pixels/grids. Note that the axis length of an ellipsoid is *half* the size of the ellipsoid in that dimension. For relatively large sized E, the difference resulted from using an ellipsoid structuring element and a 3D cube with size $(2t+1, 2s+1, 2s+1)$ is fairly small.

    Considering the close physical correspondences between ARs and extra-tropical storm systems Wernli (1997); Gimeno et al.

140 (2014), the "correct" parameter choices of t and s should be centered around the spatio-temporal scale of AR. Suppose the IVT data have a horizontal resolution of $0.75°$ and a temporal resolution of 6 hours. The typical width of an AR is within $1000\,km$ (e.g.(Guan and Waliser, 2015), and results below), therefore $s = 6\,grids$ is chosen. The typical synoptic time scale is about a week, giving $t = 4\,days$ (recall that t is only *half* the size of the time dimension). An extra grid is added to ensure an odd numbered length: the number of time steps is $4\,steps/day \times 4\,days \times 2 + 1\,step = 33\,steps$.

145   Lastly, a candidate AR is defined as a continuous region where THR anomalies are above zero, however, the IVT accounted by this candidate is the total IVT (i.e. the sum of reconstruction and anomaly, as shown in Fig. 1a). Thus detected candidates are then subject to some geometrical filtering, as introduced next.

2.2   Geometric considerations

The identified AR candidates are then subject to some geometric filtering to remove non-AR like systems such as tropical

150 cyclones. The geometric requirements include:

    1. minimum length and minimum area: the length of an AR is defined as the line integral of the AR axis, defined in the following section. A typical $2000\,km$ minimal length requirement is adopted to achieve greater compatibility with previous studies, however, a relaxed $800\,km$ threshold is also applied to allow weaker systems, many of which serve as
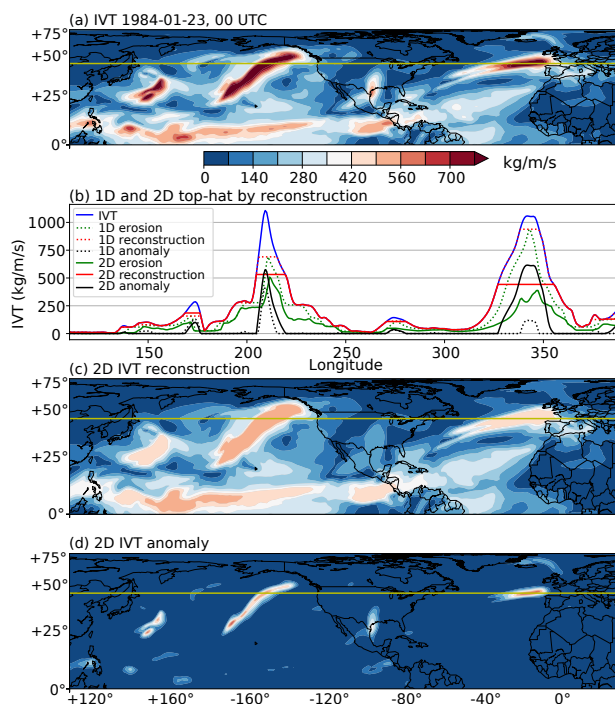
Figure 1. Illustration of 1D and 2D THR processes. (a) snapshot of IVT in $kg/m/s$ at 1984-Jan-23 00 UTC. The horizontal line denotes a zonal cross-section. (b) IVT profile along the zonal cross-section defined in (a) as blue curve. Green curves are profiles of erosions, red ones the reconstructions, and black ones the anomalies. Dashed lines show results obtained via 1D erosion/reconstruction and solid lines are results from 2D versions. (c) 2D reconstruction of IVT, in $kg/m/s$. (d) IVT anomaly defined as the difference between IVT and 2D reconstruction, in $kg/m/s$.

the genesis stage of strong ARs, to be included. This helps depict a more complete picture of AR life cycle. The exact

155   number used will be specified when showing the results. A $500 \times 10^3 \, km^2$ minimum area requirement is used to to filter out some miniature features.

2. maximum length and maximum area: when setting too low a standard in detecting AR candidates, the resultant region may cover too large an area that no longer conform to the definition of AR. A maximum length of $11,000 \, km$ and a maximum area of $10 \times 10^6 \, km^2$ are imposed to screen out such cases.

160 3. isoperimetric quotient and length/width ratio: defined as the ratio of the area enclosed by an AR candidate's boundary and that of the circle having the same perimeter of the AR: $Q = 4\pi A/L^2$, where A being area in km^2 and L being perimeter in km. This serves the same purpose as the length/width ratio typically used in previous studies, and more circular regions (such as tropical cyclones) having isoperimetric quotients greater than 0.7 are filtered out. The reason for the preference over length/width ratio is that length calculation is based on finding an AR's axis, which in turn

165   involves solving an array of optimal path-finding problems (see Section 2.3). Therefore the easier solvable isoperimetric quotient can help bypass some unnecessary computations. After isoperimetric quotient filtering, passing candidates are further filtered by a minimal length/width ratio of 2.

    4. an arbitrary latitudinal range of $23 - 80°$ is imposed on the centroid of an candidate AR to select only mid-latitude systems. The use of centroid as the metrics implies that some systems may have a tropical portion in their geographical

170   region but are primarily mid-latitude as a whole.

Passing candidates from the geometrical filtering are regarded as ARs, their spatial regions are termed "AR regions", and the appearance at an instantaneous time point constitutes an "AR occurrence", which is equivalent to the term "AR object" in (Zhou et al., 2018). The contiguous occurrences through time of a single AR entity constitute an "AR track".

2.3   Finding AR axis

175 Identifying an axis of an AR is important for tracking the movement of the AR. Here we describe a new procedure to identify the axis. The axis of an AR is sought from the binary mask (I_k) representing the spatial region of the AR. A solution in a planar graph framework is proposed here. The process of defining the nodes and edges of the graph is given in the Appendix, and an example of the axis finding algorithm is given in Fig. 2.

    The boundary pixels of the AR region are first found, labeled L_k. The trans-boundary moisture fluxes are compute as

180 the dot product of the gradients of I_k and (u_k, v_k): $\nabla I_k \cdot (u_k, v_k)$, where u_k and v_k are the vertically integrated moisture fluxes in the zonal and meridional directions, respectively. Then the boundary pixels with net input moisture fluxes can be defined as $L_{k,in} = \{p \in L_k \mid (\nabla I_k \cdot (u_k, v_k))(p) > 0\}$, similarly, boundary pixels with net output moisture fluxes is the set $L_{k,out} = \{p \in L_k \mid (\nabla I_k \cdot (u_k, v_k))(p) < 0\}$. These boundary pixels are colored in green and black, respectively, in Fig. 2.

    For each pair of boundary nodes $\{(n_i, n_j) \mid n_i \in L_{k,in}, n_j \in L_{k,out}\}$, a simple path (a path with no repeated nodes) is

185 sought that, among all possible paths that connect the entry node n_i and the exit node n_j, is the "shortest" in the sense that its path-integral of weights is the lowest. The weight for edge e_{ij} is defined as:

$$w_{ij} = e^{-f_{ij}/A} \tag{2}$$

where $f_{i,j}$ is the projected moisture flux along edge $e_{i,j}$ (see Appendix for more details), and $A = 100\,kg/m/s$ is a scaling factor. This formulation ensures a non-negative weight for each edge, and penalizes the inclusion of weak edges when a

190 weighted shortest path search is performed.

    The Dijkstra path-finding algorithm Dijkstra (1959) is used to find this shortest path p_{ij}^*. Then among all p_{ij}^*s that connect all entry-exit pairs, the one with the largest path-integral of along-edge fluxes is chosen as the AR axis, as highlighted in yellow in Fig. 2.

    It could be seen that various aspects of the physical processes of ARs are encoded. The shortest path design gives a natural

195 looking axis that is free from discontinuities and redundant curvatures, and never shoots out of the AR boundary. The weight
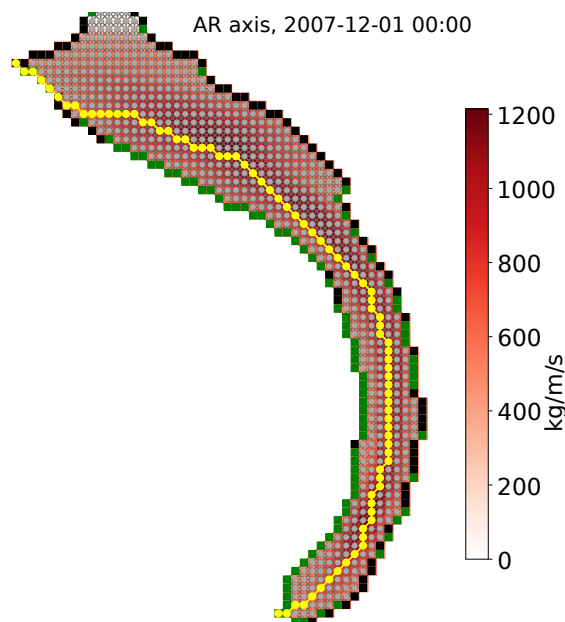
Figure 2. Application of the axis finding algorithm on the AR in the North Pacific, 2007-Dec-1 00 UTC. IVT within the AR is shown as colors, in $kg/m/s$. The region of the AR (I_k) is shown as a collection of gray dots, which constitute nodes of the directed graph. Edges among neighboring nodes are created. A square marker is drawn at each boundary node, and is filled with green if the boundary node has net input moisture fluxes ($n_i \in L_{k,in}$), and black if it has net output moisture fluxes ($n_i \in L_{k,out}$). The found axis is highlighted in yellow.

formulation assigns smaller weights to edges with larger moisture fluxes, "urging" the shortest path to pass through nodes with greater flux intensity. The found axis is by design directed, which in certain applications can provide the necessary information to orient the AR with respect to its ambiance, such as the horizontal temperature gradient, which relates to the low level jet by the thermal wind relation.

2.4 Tracking ARs across time steps

For each AR, we take seven (roughly) evenly spaced points along the AR axis as "anchors" that collectively describe the approximate location of the AR. To measure the inter-AR distances, we borrow the Hausdorff distance that is commonly used in compute vision to measure the geometrical similarity between 2D or 3D objects (e.g. (Huttenlocher et al., 1993; Vergeest et al., 2003)), and modify it as follows.

Denote the anchor points of an AR at time t as $A = \{a_1, a_2, \cdots, a_7\}$, and those of an AR at time $t+1$ as $B = \{b_1, b_2, \cdots, b_7\}$. The forward Hausdorff distance is defined as:

$$h_f(A, B) \equiv \max_{a \in A}\{\min_{b \in B}\{d_g(a, b)\}\} \tag{3}$$

namely, the largest great circle distance (d_g) of all distances from a point in A to the closest point in B. And the backward Hausdorff distance is:

$$h_b(A, B) \equiv \max_{b \in B}\{\min_{a \in A}\{d_g(a, b)\}\} \tag{4}$$

Note that in general $h_f \neq h_b$. Unlike the standard definition of Hausdorff distance that takes the maximum of h_f and h_b, we take the minimum of the two:

$$H(A, B) \equiv min\{h_f(A, B), h_b(A, B)\} \tag{5}$$

The rationale behind this modification is that merging/splitting of ARs mostly happens in an end-to-end manner, during which a sudden increase/decrease in the length of the AR induces misalignment among the anchor points. Specifically, merging (splitting) tends to induce large backward (forward) Hausdorff distance. Therefore $min\{h_f, h_b\}$ offers a more faithful description of the spatial closeness of ARs. For merging/splitting events in a side-to-side manner, this definition works just as well.

This formulation effectively summarizes inter-AR closeness into a single distance measure, therefore the tracking of ARs across time steps can be achieved using similar techniques as in the tracking of tropical cyclones or storms.

There are two possible manners that such feature tracking can performed: i) in a "simple path scheme" where the track of a feature across time forms a topological simple path, i.e. no merging nor splitting is allowed, and a system can only appear at one location at any given time. ii) in a "network scheme" where features are allowed to merge/split for arbitrary number of times, and their combined track form a directed network. The former scheme is simple to implement and suitable for occurrence statistics, as each occurrence is counted only once. In the later scheme, an occurrence may be included in more than one tracks if it is involved in a merging or splitting. Therefore, the latter scheme is more suitable for case studies where the full lifetime of a system or interactions between systems are of interest.

In this study we focus on the simple path tracking scheme. To achieve that, a nearest neighbor method is used that the two AR axes found in consecutive time steps with a Hausdorff distance $\leq 1200\,km$ are linked, with an exclusive preference to the smallest Hausdorff distance. The full algorithm is given in Appendix. Two selected cases using the network tracking scheme are given as an illustration.
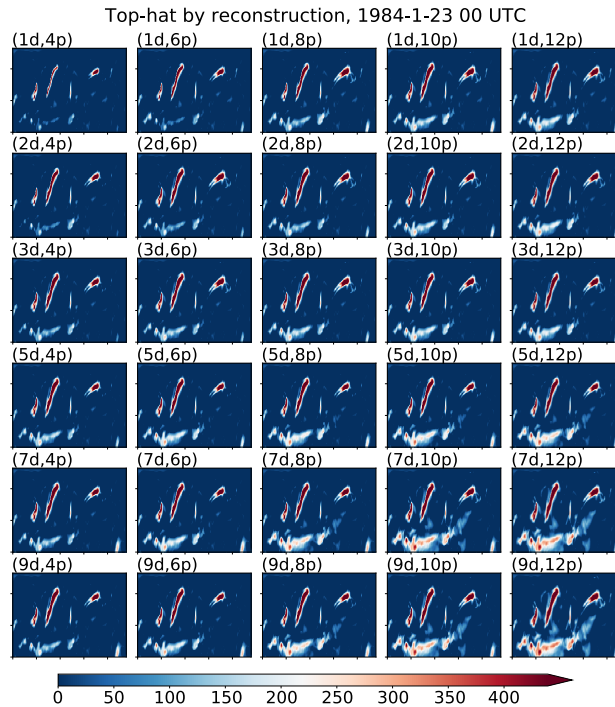
Figure 3. IVT anomalies (in $kg/m/s$) from the THR process at 1984-Jan-23 00 UTC. Subplots are results obtained using different combinations of the time (t) and space (s) parameters of the 3D structuring element in the THR process, and the subplots are labeled in a format of (td, sp), with d being short for *days* and p for *pixels*. From row 1 to row 6, t increases from $t = 1\,day$ to $t = 9\,days$. From column 1 to column 5, s increases from $s = 4\,pixels$ to $s = 12\,pixels$, with a step of 2. Axes information has been omitted for brevity, and the domain is the same as in Fig. 1a.

3 Parameter sensitivity tests in the detection of ARs

3.1 Sensitivity of AR occurrence numbers to parameters

With the geometric metrics kept constant, the parameters that affect the detection performance of the THR algorithm is the
235   temporal (t) and spatial (s) sizes of the structuring element. ARs found with a given parameter combination is labeled as $THR - tx - sy$, where x (y) denotes the value of t (s), in unit of number of days (number of grid cells).

Shown in Fig. 3 are the IVT anomalies from the THR process at 1984-Jan-23 00 UTC, obtained using 30 different combinations of t and s. The IVT data are computed as $IVT = \sqrt{u^2 + v^2}$, where u and v are the vertically integrated horizontal moisture flux components, with a $0.75\,°$ horizontal resolution and a 6-hourly temporal resolution. u and v data are obtained
240   from the ECMWF's ERA-I reanalysis product Dee et al. (2011). It has been demonstrated that the choice of reanalysis dataset contributes little to the resultant detection statistics Ralph et al. (2018); Shields et al. (2018). It can be seen that the filtering process is rather insensitive to the size/shape of the structuring element. All three major ARs and the moderate one at the center

of the map are isolated in each combination, and notable differences only appear in the tropical reservoir and around the edges of the isolated ARs. In particular, larger structuring element retains more tropical signals and gives larger AR regions. This is

245 because the spatio-temporal size of enlarged structuring element is starting to deviate away from the transient nature of ARs and would tend to include larger systems.

As a comparison, we also applied two conventional detection methods on the same ERA-I data. For the constant IVT threshold approach, IVT anomalies are first obtained by subtracting from the 6-hourly IVT data a low-frequency component, which is the mean annual cycle (during 2004-Jan to 2010-Dec period) smoothed by a 3-month moving average. The use of

250 anomalous IVT instead of absolute values helps remove slow-varying features and makes a fixed threshold more applicable across basins, seasons and years Mundhenk et al. (2016). The only parameter used in this method is the cut-off IVT value, therefore ARs found by an IVT anomaly threshold of, for instance $250\,kg/m/s$, are labeled as $IVT250ano$.

To detect ARs using a percentile-base threshold, we first computed the 85th IVT percentile for each of the 12 months within all 6-hourly time steps during the 3-month period centered on that month, within a 9-year moving time window. For instance,

255 JJA months during 1996–2004 are used to find the 85th percentiles for the month of 2000-July. Then the threshold used to detect AR candidates is the 85th IVT percentile, or a fixed $100\,kg/m/s$, whichever is larger, as in (Guan and Waliser, 2015). ARs found by this method are labeled as IVT85%.

As the parameters of THR and constant-IVT methods are of different natures (spatio-temporal scales versus horizontal vapor flux), it is not obvious how to design directly comparable perturbation ranges. Therefore the perturbation range of constant

260 IVT threshold is arbitrarily chosen to be $200-300\,kg/m/s$ – a 20% perturbation around the standard $250\,kg/m/s$ value. The perturbation of t parameter is set to $1-8\,days$, and s to $3-10\,grids$, about $50-75\%$ perturbation around the standard values of $t=4\,days$ and $s=6\,grids$. The percentile value serves the same role in affecting detection results as the constant IVT threshold, therefore only the 85th percentile result is presented as a reference.

The same set of geometric filtering is applied to results from the THR, constant IVT thresholding and the IVT85% methods.

265 The minimal length requirement is set to $2000\,km$. It is important to keep in mind that much of the sensitivity in the number of detected ARs comes from the interplay between initial detection and subsequent geometric filtering Ralph et al. (2018).

Fig. 4 shows the mean annual number of AR occurrences over the North Pacific during 2004-2010 from different methods. The numbers are the AR occurrences within all 6-hourly time steps, evenly divided into calendar years. It could be seen that the annual mean detection number displays lower sensitivity to the THR t parameter at fixed s (Fig. 4a), and similarly to the s

270 parameter at fixed t (Fig. 4b), compared with the sensitivity to IVT thresholds (Fig. 4d). Detection number varies more when both t and s change simultaneously, as shown in Fig. 4c, from 2208 at the smallest ($t=1\,day$, $s=3\,grids$) scale, to 2730 at the ($t=6\,days$, $s=8\,grids$) scale. The tendency of increasing AR numbers with enlarging scales is due to the interplay between initial detection and geometric screening. However, as long as the parameters are set around the typical synoptic spatio-temporal scales, the resultant AR occurrence numbers are more or less the same.

275 In comparison, the constant IVT threshold method produces fewer ARs as one raises the threshold, creating a drop of 848 from the IVT200ano to the IVT300ano setup. The effect from varying IVT thresholds is intuitive: as one raises the threshold, smaller regions are retrained. When coupled with a minimal size requirement, more get filtered out.
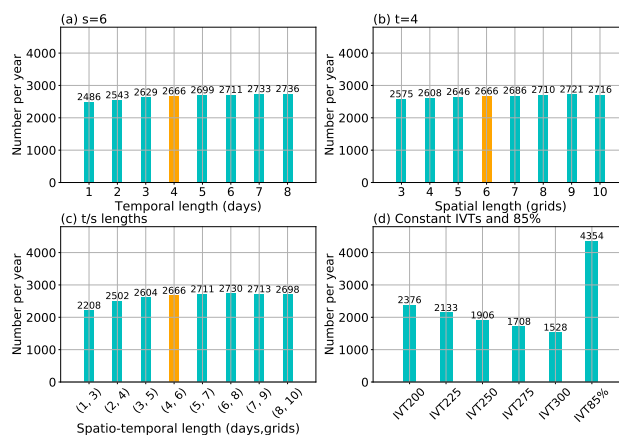
Figure 4. Average annual number of AR occurrences over the North Pacific during 2004–2010. (a) AR occurrence numbers by the THR method with various time (t) parameters and a fixed space parameter ($s = 6$). (b) similar as (a) but for fixed time ($t = 4$) and varying space (s) parameters. (c) results from the THR method with time (t) and space (s) varying simultaneously from the lower bound of $t = 1\,days, s = 3\,grids$ to the upper bound of $t = 8\,days, s = 10\,grids$. (d) AR occurrences from constant IVT thresholding method with the threshold value ranges from 200 to $300\,kg/m/s$, and the result from the IVT85% method as the last column.

Also note that the IVT85% method reports more than double the number of ARs of the highest THR method (Fig. 4d). As will be shown in later sections, this method tends to produce ARs with notably different features as the other two, and is likely

280   due to that the geometric metrics listed in Section 2.2 are insufficient in effectively filtering some weak plumes. Specifically, it is likely that the requirement of a minimal mean poleward IVT component and mean IVT direction being within $45°$ of the AR shape orientation that are applied by (Guan and Waliser, 2015) but absent in this study, that is making the greatest difference.

Results in Fig. 4 suggest that the THR-t4-s6 method reports 760 more AR occurrences per year than the IVT250ano method. By applying a matching method based on areal overlap ratio, we are able to give a closer look at the degree of agreement

285   between these two methods in term of AR occurrences and their accounted IVTs. Details of which are beyond the scope of this study and are presented in a companion work submitted separately. Some selected cases of these exclusive THR ARs are shown below.

3.2 Comparison of selected cases

Fig. 5 shows some selected cases where an AR occurrence is detected by the THR-t4-s6 method but not by IVT250ano.

290   ARs found by the former are drawn in solid green contours, and the latter in solid black contours. At 2006-01-11 06 UTC (Fig. 5a), both methods detect the stronger AR over the Northeastern Pacific, however the weaker one at $\sim 160°E$ is missed by IVT250ano. This is because the region where IVT anomalies are above the $250\,kg/m/s$ threshold is too small, as indicated by the hatching. This AR is not detected by IVT250ano until 2006-01-12 12 UTC, at which time it has migrated to $\sim 180°E$.
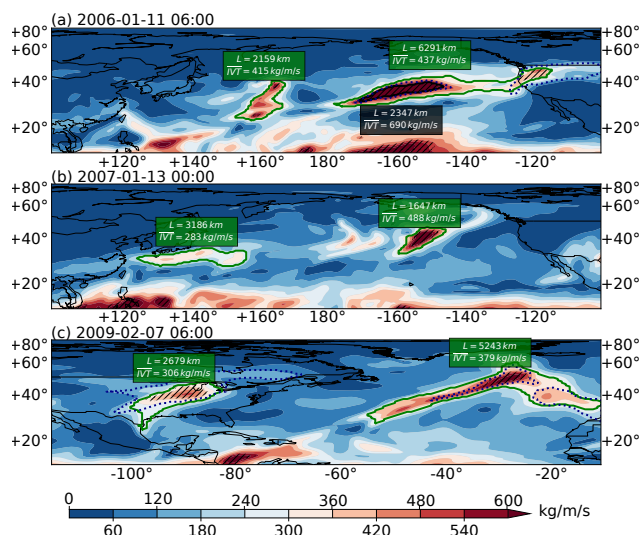
Figure 5. Snapshots of IVT distributions at (a) 2006-01-11 06 UTC over the North Pacific, (b) 2007-01-13 00 UTC over the North Pacific, and (c) 2009-02-07 06 UTC over the North Atlantic. ARs found by the THR-t4-s6 method are drawn in solid green contours, those by the IVT250ano method in solid black contours, and IVT85% in dotted black contours. Length (in km) and area-averaged IVT (in $kg/m/s$) for the THR-t4-s6 (IVT250ano) ARs are labelled out in green (black) boxes. Hatching indicates areas where the IVT anomalies are above the $250 \, kg/m/s$ threshold.

Four days later (2006-01-16 12 UTC) it makes landfall onto the North America continent. Fig. S1 in Supplementary shows the
295 entire life cycle sequence of this AR.

Similarly, the Northwestern Pacific AR at 2007-01-13 00 UTC is missed by the IVT250ano method (Fig. 5b). The THR method identifies this AR occurrence as one with a length of $3186 \, km$ and an average absolute IVT of $283 \, kg/m/s$. 30 hours later, IVT250ano detects this AR till 2007-01-18 06 UTC, at which time it is just about to make North America landfall (Fig. S2). Meanwhile, THR traces this particular AR throughout this period till one day after it is last seen in the IVT250ano
300 detection (Fig. S2). Also shown in Fig. 5b is another AR occurrence at $\sim 155°W$ that is solely detected by THR. This AR is not detected by IVT250ano until 2007-01-15 06 UTC (Fig. S2).

Fig. 5c shows another case in the North Atlantic. The AR in question is propagating over the eastern North America at the time of 2009-02-07 06 UTC. The life cycle sequence in Fig. S3 indicates that this AR never appears in the IVT250ano detection till its dissipation at 2009-02-13 12 UTC just south of Iceland. Fig. 5c also shows another AR occurrence over the
305 Northeastern Atlantic that is missed by the IVT250ano method but detected by THR.

It could be seen that the exclusive THR AR detections tend to correspond to the genesis or dissipating stages of some well-defined AR tracks (Fig. 5a,b), or in other cases the entire life cycle of some weak systems as in Fig. 5c. (Ralph et al., 2018) also suggested that discrepancies among methods are smaller in cold season than in warm season, in more active years than in

quieter years, and during time steps with higher observed IVT than those with lower IVT. In summary, sensitivity to detection
310   methods is much greater for weaker systems.

It was also observed that methods with more restrictive geometrical criteria tend to report fewer detections compared with
those with comparable magnitude thresholds but are more permissive in the geometrical requirements Ralph et al. (2018).
In most of the existing detection methods, geometrical filtering is applied as an extra step after the initial region detection.
However, these two steps are inherently closely coupled: once the candidate region is determined, so is its geometry, and with
315   the help of a sensible length estimate, its length as well. Therefore, for a magnitude thresholding detection method, the choice
of the threshold to some extent already determines the expected geometrical extent of the passing candidates, with largely
predictable behavior as one adjusts the threshold: raising the threshold level restricts the sizes of the detected ARs and vice
versa. However, what is less predictable is the resultant AR statistics when applying the same threshold to data across multiple
decades when low frequency drifts may be present, or to climate projections where different model biases are to be expected.

320   The sensitivity and uncertainty embedded in geometrical constraints still exist in the THR method, but to a much lesser
extent. Weaker systems as shown in Fig. 5 are more likely to be detected together with those most intensive ones. It also
implies that the geometrical filtering is more of an independent criterion rather than closely coupled with the initial region
detection process. This allows the inclusion of systems that are weaker (note that in climate scale, or with different model
biases, it is less obvious how weak is weak) in intensity but sizable in geometry. As shown above and will be discussed later,
325   this often leads to the captured AR tracks have fuller life cycle. As the strength and size criteria are decoupled, the user can still
apply a subsequent magnitude filtering on the maximum and/or average IVT to obtain the subset of a certain intensity level.
Therefore it offers greater control power without completely breaking the compatibility with existing methods.

As a reference, Fig. 5 also shows as dotted black contours the ARs detected by the IVT85% method. This method displays
improved sensitivity to weaker IVT signals, as in the case of the landfalling AR in Fig. 5a, and the one over the eastern North
330   America in Fig. 5c. However, it still misses the three ARs in Fig. 5a and b. Also note that the THR ARs on the eastern side
of the map in Fig. 5a and Fig. 5c enclose more than one local IVT maxima in their region contours. This can happen when a
merging or splitting creates two nearby transient plumes, and can subsequently contribute to the geometry-related uncertainties.
A method has been developed to separate such "multi-core systems" into "single-dome" ARs, and will be introduced in a future
update of the algorithm.

335   **3.3   Sensitivity of AR shapes and IVT intensities to parameters**

Some geometrical features and IVT intensities of the ARs identified in by the three methods are summarized in Fig. 6. Considering the low sensitivity to either t or s parameter with the other one fixed in the THR method, only the parameter combinations
when both t and s vary simultaneously are included.

Fig. 6 shows that enlarging the THR structuring element tends to produce ARs with larger sizes, and this can be seen in the
340   length (Fig. 6a), width (Fig. 6b) and area (Fig. 6c) distributions. (Note that width is defined as the effective width, i.e. the ratio
of area over length). However, the length/width ratio remains about constant (Fig. 6d). Raising the constant IVT threshold has
the opposite effect that the resultant ARs are progressively shorter (Fig. 6a), narrower (Fig. 6b) and smaller in size (Fig. 6c).
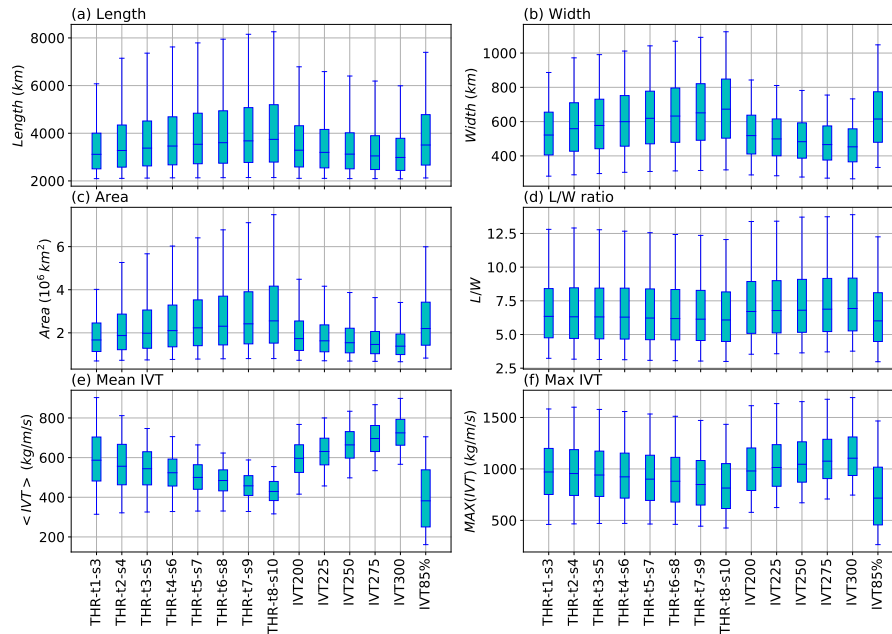
Figure 6. Distributions of (a) AR length (in km), (b) width (in km), (c) area (in $10^6\,km^2$), (d) length/width ratio, (e) mean IVT averaged over AR region (in $kg/m/s$) and (f) maximum IVT within AR region (in $kg/m/s$) of ARs identified by different methods, during the period of 2004–2010. Box ends denote the inter-quantile-range of the distribution, with the median as the line in the middle. Box whiskers denote the 5th and 95th percentiles.

Fig. 6e suggests that larger sized ARs tend to have lower mean IVT values, and this is true among THR and constant IVT threshold methods. Although the maximum IVT follows the similar trend (Fig. 6f), the differences are much smaller. This is

345 because when taking the average over the region of larger sized ARs, the mean values get "diluted" more during the spatial averaging process, yet the maximum values are largely immune to this "dilution". Therefore, the lower mean IVT values of THR ARs are primarily due to their larger sizes than due to the inclusion of weaker systems. The variation among constant IVT threshold methods is also consistent with Shields et al. (2018) that higher threshold on IVT produces higher average IVT intensities.

350 Results of the IVT85% ARs are also displayed as a reference. ARs found by this method display comparable size distributions as that by THR-t2-s4 method (Fig. 6a-d), but with notably weaker mean (Fig. 6e) as well as maximum IVT distributions (Fig. 6f). Combined with the high number of ARs found by IVT85% as shown in Fig. 4d, it could be inferred that a good number of these are fairly weak systems that get ignored by the other two.

The sizes of ARs constitute an important source of uncertainty in many AR-related estimates Ralph et al. (2018); Shields

355 et al. (2018). For instance, (Rutz et al., 2014) showed that by lowering the IVT threshold from 300 to $200\,kg/m/s$, the resultant landfalling AR frequency onto the North America coast rises by $\sim 50\%$ (see their Fig. 5). A similar concern was also raised in (Mundhenk et al., 2016) when quantifying North Pacific AR frequencies. Currently no metrics has been developed to
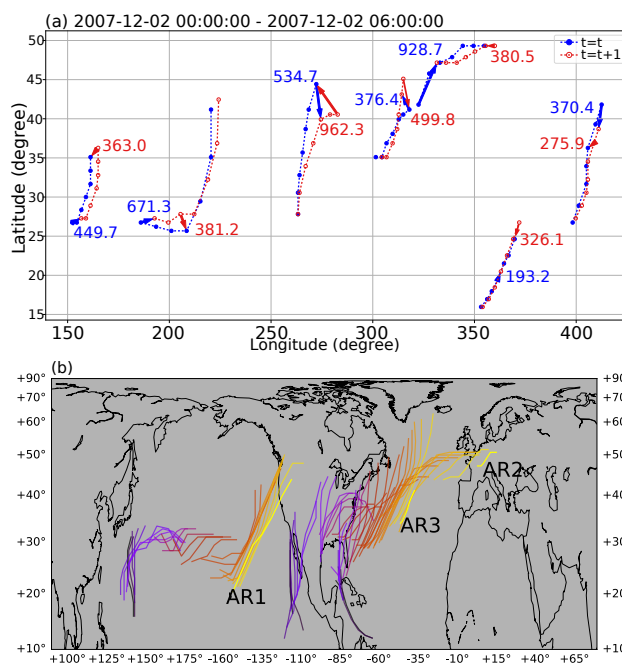
Figure 7. (a) Tracking of ARs across 2007-12-02 00 and 06 UTC using the nearest neighbor algorithm. ARs at 2007-12-02 00 are represented by their anchor points joint by dashed lines and are drawn in blue, and ARs at 2007-12-02 06 are drawn in red. Blue (red) arrows indicate the forward (backward) Hausdorff distance among paired ARs, and the distances (in km) are labeled nearby. (b) Tracks of three selected ARs represented by their axes. Life cycle of an AR is represented as the black-yellow transition in the coloring. Other ARs during the same period are omitted for brevity.

objectively quantify the appropriateness of the AR boundary definition. We offer some brief discussions on this topic from a segmentation cost perspective in the Appendix.

4   Tracking ARs across time

Besides the quantification of AR occurrences, prediction of ARs also requires tracking ARs across time steps. Fig. 7a shows an example of the tracking algorithm applied on THR-t4-s6 ARs found at 2007-12-02 00 and 06 UTC, drawn with blue and red dashed lines, respectively. Blue (red) arrow indicates the forward (backward) Hausdorff distance between a pair of ARs that get linked. It could be seen that for pairs that are well separated or relatively clustered, the Hausdorff distance correctly measures the inter-AR closeness, and enables the nearest neighbor algorithm to make the correct associations. Note that the minimal length requirement is relaxed to $800\,km$, but it is required that the same AR reaches $\geq 2000\,km$ for at least one time step during its life time.
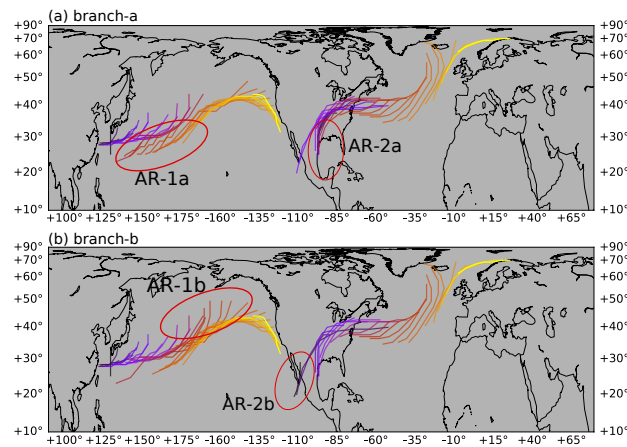
Figure 8. Tracks of two ARs obtained using the network scheme. Each of the two ARs (AR-1 and AR-2) has two branches (branch-a and branch-b) in their tracks, shown in (a) and (b) respectively. Same color scheme as in Fig. 7 is used to represent their life cycles. The different branches of a single AR track are highlighted in red ellipses.

Fig. 7b shows the tracks of three selected ARs in Nov-Dec of 2007 obtained using the simple path scheme. The axes of the ARs are drawn with a black-yellow color scheme, with the transition representing the stages of their life cycle. The two ARs

370 originated from Pacific (AR1, AR2) have experienced the association process as shown in Fig. 7a. AR1 reaches a length of $\sim 4700\,km$ shortly before its landfall onto the western coast of the North America at 2007-12-04 06 UTC. AR2 starts as an Eastern Pacific system at 2007-12-01 00, and survives the cross-continent and cross-basin travel before its European arrival at 2007-12-07 06 UTC, at which point the AR has shrunk to a fairly short $960\,km$. AR3 is initially fueled by a tropical cyclone in the Caribbean Sea and is joint by another plume (not shown in this figure) coming from the Eastern Pacific during its eastern

375 America travel, and dissipates half way through its North Atlantic propagation.

Fig. 8 shows two selected AR tracks obtained using the network scheme, where merging and splitting are captured. To achieve this, three consecutive applications of the nearest neighbor algorithm are performed, with different input arguments each time. More details are given in the Appendix. The first selected case (AR-1) starts from the Northwest Pacific at 2007-12-21 12 UTC, and splits into a southern branch (AR-1a, shown in Fig. 8a) and a northern branch (AR-1b, Fig. 8b) during

380 its eastward propagation. The two branches then merge into one shortly before the North America arrival at 2007-12-29 12 UTC. In fact, the life story of this AR is further complicated by the joining of a third branch originated from another tropical system. We have omitted the third branch for the sake of clarity. AR-2 demonstrates a merging case that a system from the Gulf of Mexico (AR-2a, Fig. 8a) is joint by an Eastern Pacific one (AR-2b, Fig. 8b) and the combined track then makes European landfall. It has been estimated that about $25\,\%$ of wintertime extra-tropical cyclone tracks experience at least one

385 merging and/or splitting during their life time Hanley and Caballero (2012). The proposed method enables similar analysis on AR tracks, and their possible links with merging or splitting cyclones.
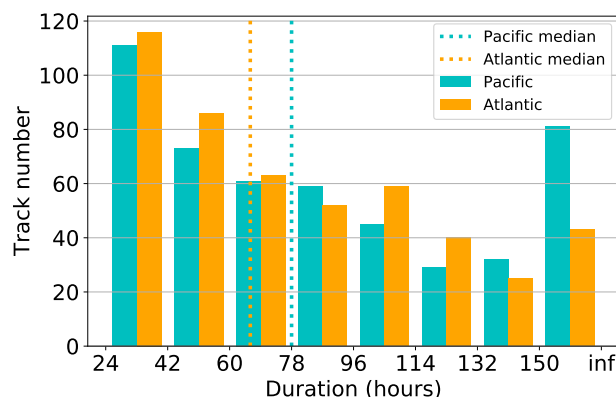
Figure 9. Distribution of track durations (in hours) of AR tracks in the North Pacific (cyan) and North Atlantic (orange).

The simple path scheme is then applied to all Northern Hemisphere ARs found by the THR-t4-s6 method during the Nov-April seasons of 2004-Nov to 2010-April. Depending on the AR centroid at genesis time, those lying within $120\,^{\circ}E - 100\,^{\circ}W$ are labeled Pacific, and those within $100\,^{\circ}W - 20\,^{\circ}E$ are labeled Atlantic. After removing tracks lasting shorter than 24 hours,

390   it is found that on average, both North Pacific and North Atlantic have about 80 AR tracks during the Nov-April season. More notable difference is observed in track durations , as shown in Fig. 9. The median of Pacific track durations is 78 hours, that of Atlantic is 66 hours. Such a difference is largely attributed to those tracks lasting for 150 hours or beyond, and is consistent with the greater longitudinal span of the Pacific basin. Note that the duration is defined as the lifetime of individual AR tracks and is distinct from a per-grid, Eularian definition as in, for instance, (Guan and Waliser, 2015; Rutz et al., 2014, 2015; Sellars

395   et al., 2017), which measured the contiguous time spans when a grid cell experiences AR occurrences.

Fig. 10 displays the movements of all North Hemisphere AR tracks during the Nov-April seasons of 2004-Nov to 2010-April. The geometrical centroid of the AR region is used as a proxy to location, and coloring represents the maximum IVT within the AR region at each time step. It could be seen that distributions of AR tracks overlap well with the storm track regions of the North Pacific and North Atlantic basins, with a southwest-northeast orientation Hodges (1994). ARs of both ocean basins can

400   be traced back to the western boundary warm current regions - the Kuroshio current for Pacific and Gulf Stream for Atlantic. For Atlantic, a considerable number of ARs also originate from the Gulf of Mexico.

Note that Fig. 10 also shows an additional hot spot in the middle east around the Red Sea, one across the North Africa-Mediterranean-Eastern Europe, and another even weaker one over west Siberia. We would refrain from naming them ARs, as they conflict with the conventional AR definition in that they are weaker in strength, not ocean-originated and are likely driven

405   by different physical mechanisms. However, these are well organized (above thousand kilometers in length) and relatively persistent (can be tracked over 24 hours) water plumes. The identification of such systems speaks to the greater adaptability of the THR method, and its ability in encompassing a wider range of transient water vapor plumes in a single framework.
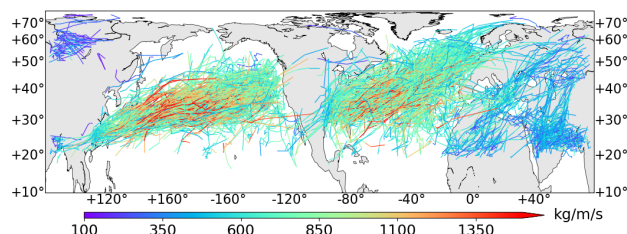
Figure 10. Movement of North Hemisphere AR tracks as indicated by the geometrical centroids during the Nov-April seasons of 2004-Nov to 2010-April. Color represents the maximum IVT within the AR region.
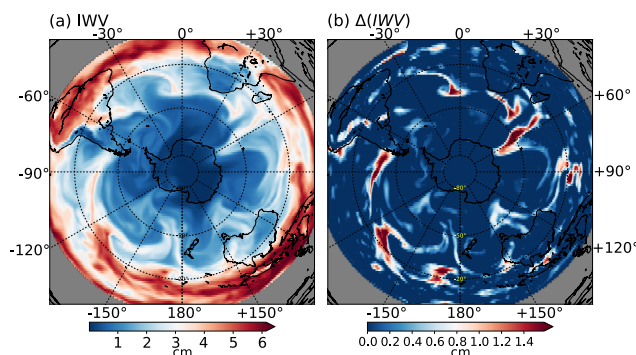
Figure 11. (a) IWV in the Southern Hemisphere at 2009-05-19 00 UTC, in cm. (b) IWV anomalies in cm, obtained using a 2-step THR, which uses a structuring element E with size $t = 4\,days$, $s = 6\,pixels$.

5 Application on IWV in polar region

To support our claim that the proposed THR method can be extended to IWV-based applications, we show only a selected

410   case of IWV-based AR detection here because of the length limitation of the paper. Unlike IVT where the transition from tropical trades to extra-tropical westerlies creates a natural separation in the tropical and extra-tropical IVT distribution, ARs represented by IWV are usually well connected with the tropical reservoir. Therefore some modification of the THR process is needed. The detailed procedure is given in Appendix. A selected case is shown in Fig. 11.

     The IWV data from ERA-I are first projected onto the Polar Lambert Azimuthal projection before carrying out the 2-step

415   THR process, which uses the same structuring element of size $t = 4\,days$, $s = 6\,pixels$. Shown in Fig. 11a and b are the IWV and IWV anomalies respectively, at 2009-May-19 00 UTC. The AR located at $60\,^\circ E$ is marching towards the Antarctica. This particular case has been documented by (Gorodetskaya et al., 2014), in which the conventional $2\,cm$ threshold value for IWV has been corrected by an empirical formula to cater to the decreased saturation capacity of the polar region. Note that although IVT is more than two orders of magnitude larger than the values of IWV, the THR method does not require a separate threshold

420   for the IWV applications, and no polar adjustment is needed.

6   Conclusions

In this work we propose a new set of automated AR detection and tracking methods. The THR algorithm exploits the transient nature of ARs to segment IVT signals. Compared with the intensities of AR-related vapor fluxes, the inherent spatio-temporal scale of AR is a more stable attribute. This makes the method less prone to the potential difficulties in reliably detecting ARs in a warming climate, and results from different models more directly comparable when model biases may be present. It also demonstrates reduced sensitivity to parameter choices, and greater tolerance to a wider range of transient water vapor plumes, and therefore has the potential of encompassing water plumes with various strengths into a unified framework. Furthermore, as strength is decoupled from the initial selection process, it is subject to the user to later select only those that meet a given strength standard, giving finer control power for different applications.

An intensity scale like those used to rank tropical cyclones has just been established for the landfalling ARs Ralph et al. (2019). In the proposed scale, five intensity categories were devised, covering the lowest "weak" category with observed IVT being $250 - 500\,kg/m/s$, to the highest "exceptional" category whose IVT level is $1250\,kg/m/s$ or above, with extra duration factors taken into account in all categories. The difference in categories can mean the difference from a mild, beneficial atmospheric fresh water delivery to a hazardous extreme event that can cause damages measured in billions of dollars Ralph et al. (2019). Therefore, it is advantageous for a detection method to have a wider detection spectrum, rather than solely focusing on the most intensive events.

Besides the mostly commonly used magnitude thresholding methods, new AR detection techniques are continually being developed. For instance, the ARTMIP project reported one machine learning based detection method that is also threshold-free Shields et al. (2018). As the AR research matures, more inspirations from other disciplines like machine learning, image processing or computer vision are brought into the view of the AR community. Such inputs can offer some new perspectives of looking at various AR-related questions, and can often lead to new discoveries that would have been obscured using conventional methods.

More physical information is encoded into the axis finding method based on a directed graph model, creating an effective summary of an AR in the sense of geometry and physics. Problems of discontinuity, spurious branches, weak physical correspondences and difficulties in handling complex shapes are overcome in this method.

Lastly, tracking of ARs across time steps in a similar manner as the tracking of tropical cyclones and storms is achieved using a modified Hausdorff distance as the inter-AR proximity measure. Long-lived ARs spanning multiple days, having cross-continent or cross-basin tracks can be reliably traced through their tropical/sub-tropical origins to high-latitude landfalls.

However, these methods come with their own limitations. Firstly, the THR method is considerably more complex than the constant thresholding method. Although it has been shown to have lower parameter sensitivity, sensitivities in other aspects still exist, particularly in the interplay between candidate region detection and the subsequent geometric filtering. Some ARs may fail the detection for their being just shy of a $2000\,km$ length requirement, or in other cases being too long because two nearby water plumes are merged together. Ambiguity in the shape of ARs still constitutes an important source of uncertainty in many AR-related statistics. A more accurate and controllable depiction of the AR shape is still in demand.

455 *Code and data availability.* The ERA-I Reanalysis data used in the manuscript is publicly available. The implementations of the algorithms used in this work in the Python programming language is posted at the Zenodo repository (XU et al., 2020).

Appendix A

This appendix provides more technical details on AR detection using the THR algorithm, AR axis definition, inter-AR distance measure and tracking algorithms. A discussion on the AR sizes from a segmentation cost perspective is also given. Some select
460   AR life cycle sequences are shown at the end.

A1   Top-hat reconstruction by dilation algorithm

Greyscale reconstruction by dilation can be defined as iterative applications of elementary geodesic dilations of a marker image M "under" a mask image I till convergence Vincent (1993). An elementary geodesic dilation is defined as:

$$\delta_I^{(1)}(M) = (M \oplus B) \wedge I \tag{A1}$$

465   where $M \oplus B$ is the dilation of M by a flat structuring element B, and $\wedge$ is pointwise minimum operator. Intuitively, geodesic dilation spreads local high intensity value in the marker image M to its neighbors so long as it does not exceed values in the "mask" image I. The spread starts from the given "marker" and stops till no change can be made:

$$\delta_I^{(n)}(M) = \underbrace{\delta_I^{(1)} \circ \delta_I^{(1)} \circ \cdots \circ \delta_I^{(1)}(M)}_{n\,times}, \; such \; that$$

$$\delta_I^{(n)}(M) = \delta_I^{(n+1)}(M)$$

470   where $\delta_I^{(n)}(M)$ is the reconstruction by dilation.

The "marker" image used is the greyscale erosion of the image I by a structuring element E:

$$M \equiv \epsilon_E(I) = I \ominus E \tag{A2}$$

The erosion and reconstruction by dilation computations are performed using the scikit-image software package van der Walt et al. (2014) designed for imaging processing in the Python programming language.

475   **A2   Define the directed planar graph for axis finding**

A directed planar graph is built from I_k, which is the binary mask defining the AR region, using the coordinate pairs (λ_k, ϕ_k) as nodes (see Fig. A1 for an illustration). At each node, directed edges to its eight neighbors are created, so long as the moisture flux component along the direction of the edge exceeds a user-defined fraction (ϵ) to the total flux. The along-edge flux is defined as:

$$480 \quad f_{ij} = u_i \sin(\alpha) + v_i \cos(\alpha) \tag{A3}$$
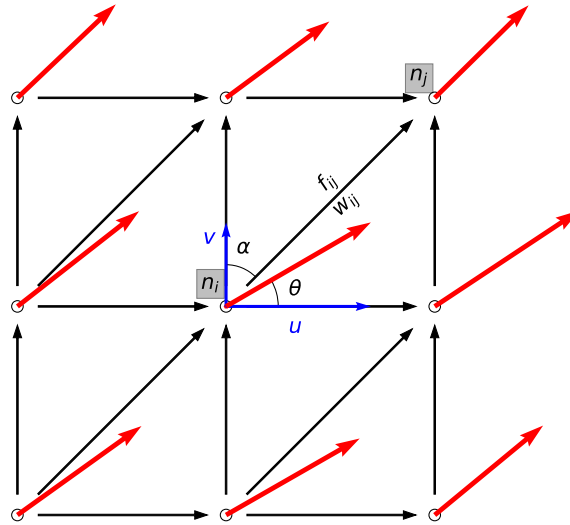
Figure A1. Schematic diagram illustrating the planar graph built from the AR pixels and horizontal moisture fluxes. Nodes are taken from pixels within region I_k, and are represented as circles. Red vectors denote IVT vectors. The one at node n_i forms an angle θ with the x-axis, and has components (u, v). Black arrows denote directed edges between nodes, using an 8-connectivity neighborhood scheme. The edge between node n_i and n_j is e_{ij}, and forms an azimuth angle α with the y-axis. w_{ij} is the weight attribute assigned to edge e_{ij}, and f_{ij} is along-edge moisture flux.

where f_{ij} is the flux along the edge e_{ij} that points from node n_i to node n_j, and α is the azimuth angle of e_{ij}.

Therefore an edge can be created if $f_{ij}/\sqrt{u_i^2 + v_i^2} \geq \epsilon$. Here a relatively small $\epsilon = 0.4$ is used, as the orientation of an AR can deviate considerably from its moisture fluxes, and denser edges in the graph allows the axis to capture the full extent of the AR.

485 ## A3 Tracking ARs using simple path scheme

To make an association between two ARs at consecutive time steps, a "nearest neighbor" approach is used. Formally, suppose n tracks have been found at $t = t$: $A = \{a_1, a_2, \cdots, a_n\}$, and $t = t+1$ has m new records: $B = \{b_1, b_2, \cdots, b_m\}$. The Hausdorff distances between all pairs of possible associations form a distance matrix:

$$M = \begin{bmatrix} H(a_1, b_1) & H(a_1, b_2) & \cdots & H(a_1, b_m) \\ H(a_2, b_1) & H(a_2, b_2) & \cdots & H(a_2, b_m) \\ \vdots & \vdots & \vdots & \vdots \\ H(a_n, b_1) & H(a_n, b_2) & \cdots & H(a_n, b_m) \end{bmatrix} \quad (A4)$$

Algorithm 1: Nearest neighbor algorithm

Data: A: list of existing tracks at t, B: list of new records at $t+1$, M: distance matrix, H^*: maximum allowed distance, R^-: list of indices of tracks not allowed to link, C^-: list of indices of records not allowed to link.

Result: A: updated list of tracks. R^+: list of indices of tracks get linked. C^+: list of indices of records get linked.

```
 1  create empty lists R+ = [] and C+ = [];
 2  while min(M) < H* and len(R+) < min(n, m) do
 3      for each (i, j) that M(i, j) = min(M) do
 4          if i ∉ R⁻ and j ∉ C⁻ then
 5              let a_i = A[i];
 6              let b_j = B[j];
 7              if time stamp of b_j = latest time stamp of a_i then
                    /* relevant for network scheme only;
                       the track has got a new record, splitting happening;
                       retrieve the original a_i                              */
 8                  let a_i = A'[i];
                    /* make a new track                                       */
 9                  append a_i to A;
10              end
11              add i to R+;
12              add j to C+;
13              add i to R⁻;
14              add j to C⁻;
15              append b_j to a_i;
16              let M(i, j) := ∞;
17          else
18              let M(i, j) := ∞;
19          end
20      end
21  end
```

Figure A2. Nearest neighbor algorithm

490   Then Algorithm A2 is called with these arguments: $(A = A, B = B, M = M, H^* = 1200\,km, R^- = [], C^- = [])$. The algorithm iteratively links two AR records with the smallest distance, so long as the distance does not exceed a given threshold H^*. It ensures that no existing track connects to more than one new records, and no new record connects to more than one existing tracks. After this, any left-over records in B form a new track on their own. Then the same procedure repeats with updated time $t := t + 1$. Tracks that do not get any new record can be removed from the stack list, which only maintains a few active

495   tracks at any given time. Therefore the complexity does not scale with time.

A4   Tracking ARs using network scheme

Merging and splitting are allowed in this scheme and the process consists of three consecutive applications of the nearest neighbor algorithm described above. Specifically, the process works as:

1. Make a copy A' of the existing tracks A at time $t = t$, and a copy M' of the distance matrix M.

500   2. Apply the nearest neighbor algorithm as in Algorithm A2:

$$A, R_1^+, C_1^+ = Algorithm\ A2(A = A, B = B,$$
$$M = M, H^* = H^*, R^- = [], C^- = []) \tag{A5}$$

Where R_1^+ (C_1^+) contains the indices of tracks (records) that are linked in this process.

3. Merging is handled by repeating the nearest neighbor process as:

$$A, R_2^+, C_2^+ = Algorithm\ A2(A = A, B = B,$$
$$M = M', H^* = H^*, R^- = R_1^+, C^- = [])$$
(A6)

Note that the backed-up distance matrix M' is used as it contains no infinities, and the argument $R^- = R_1^+$ masks out tracks that have been linked in the previous step, giving other tracks a chance to *merge* to the same new record.

4. Splitting is handled by repeating the nearest neighbor process as:

$$A, R_3^+, C_3^+ = Algorithm\ A2(A = A, B = B, M = M',$$
$$H^* = H^*, R^- = [], C^- = C_1^+ \cup C_2^+)$$
(A7)

This time, new records that have been allocated in the previous steps are masked, giving other records a chance to *split* an existing track. Note that when splitting, the new record is appended to a back-up copy of the track from A', and a new track is added to A after the split, as described in line 7-9 of Algorithm A2.

5. Any left-over records in B form a new track on their own. Then return back to step 1 with updated time $t := t + 1$.

It should be noted that this is not equivalent to a "link-all-neighbors" strategy, which will deny the preference to the nearest neighbor and create redundant links before (after) a merge (split). After a merge, merging tracks will have identical tracks thereafter; and for every split, a new track is created with its history retained. Therefore there would be many duplicated records in this scheme.

A5   Segmentation cost estimates

The AR detection task can be viewed as a segmentation problem in the image processing framework that a segment of the image (AR) is identified as the foreground image and thus getting separated from its background (the IVT distribution). In this formulation, a cost function can be defined to quantify the total intra-segment-variances, as an evaluation of the effectiveness of the AR detection method in isolating high AR-related IVT values from its background:

$$C \equiv \frac{1}{IVT_{max}(N_f + N_b)}[\sum_{N_f}(I_{f,i} - \overline{I_f})^2 + \sum_{N_b}(I_{b,i} - \overline{I_b})^2]$$
(A8)

where N_f, N_b are the number of grids in the foreground and background segments, respectively. $I_{f,i}$ ($I_{b,i}$) denotes the pixel value of the foreground (background) image at location i, and the average across the segment is denoted $\overline{I_f}$ ($\overline{I_b}$). The summations in square brackets quantify the total intra-segment-variances. This is the same definition as used by Otsu (1979)
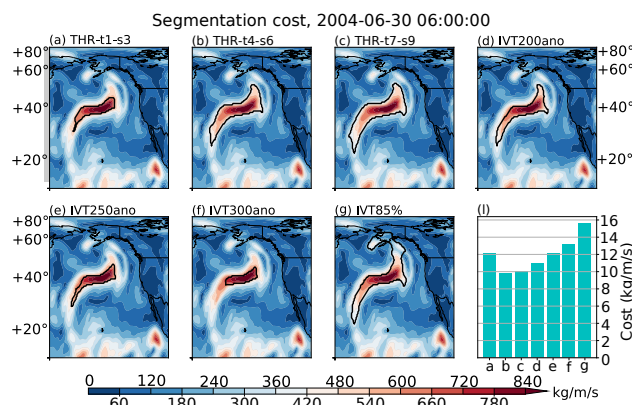
Figure A3. IVT distribution at 2004-06-30 06 UTC over the Northeastern Pacific (in $kg/m/s$). Boundaries of ARs detected by (a) THR-t1-s3, (b) THR-t4-s6, (c) THR-t7-s9, (d) IVT200ano, (e) IVT250ano, (f) IVT300ano and (g) IVT85% methods are drawn with black curves. (i) the segmentation costs in all seven methods, in $kg/m/s$.

in determining the optimal segmentation threshold. Either too small or too large an AR boundary definition would raise the cost function, and result in a less effective separation of high intensity values from the background. This is also equivalent to the cost function used in the k-means clustering algorithm (e.g. (Dreyfus, 2005, chap. 7), in this case the number of clusters is $k = 2$) where the minimization of the cost converges to the solution. The normalization by maximum IVT (IVT_{max}) and the

530   total image domain size ($N_f + N_b$) enables inter-comparisons among different ARs. The total image domain is chosen as the bounding box of the AR boundary expanded out in four directions by five grid cells.

Fig. A3 compares the segmentation costs of an AR mutually detected by three THR methods, three constant IVT threshold methods and the IVT85% method, at 2004-June-30 06 UTC over the Northeastern Pacific. Consistent with discussions in the main text, shrinking the THR structuring element has a similar effect as raising the constant IVT threshold that a smaller

535   proportion of the transient IVT anomalies is segmented from the background. This particular time step is chosen because the segmentation cost comparison as shown in Fig. A3i is qualitatively consistent with the long-term 2004–2010 average (not shown). Although not specifically designed to minimize the segmentation cost, the THR-t4-s6 method that reflects the typical spatio-temporal scale of ARs gives the lowest cost.

A6   2-step THR for IWV polar application

540   Unlike IVT where the transition from tropical trades to extra-tropical The 3D erosion process is the same as for IVT, but instead of performing the reconstruction in three dimensions simultaneously, reconstruction on IWV is split into two consecutive steps.

The first one uses a structuring element B that has only non-zero values along the time dimension. This constrains the geodesic dilation to the time dimension. Formally, this step involves:

$$\begin{cases} \delta(IWV)_t = & \delta_{IWV}^{(n)}(IWV \ominus E) \\ \Delta(IWV)_t = & IWV - \delta(IWV)_t \end{cases} \tag{A9}$$

545   The second step takes $\Delta(IWV)_t$ as input, and performs a THR process in which geodesic dilation only expands in x- and y- dimensions.

$$\begin{cases} \delta(IWV)_s = & \delta_{\Delta(IWV)_t}^{(n)}(\Delta(IWV)_t \ominus E) \\ \Delta(IWV) = & \Delta(IWV)_t - \delta(IWV)_s \end{cases} \tag{A10}$$

Recall that the THR algorithm achieves segmentation according to the spatio-temporal "spikiness" of the data. As ARs in IWV are only *spatially* connected to the tropical reservoir which is *temporally* much more persistent, they can be separated in

550   the time dimension THR. Then the second THR is concerned with spatial dimensions, and helps retaining spatially transient features. Alternative to the 2-step THR approach, a temporal filtering can be used to suppress the tropical signals. Then a similar 3D THR process can be applied on the high-pass component of IWV.

Author contributions. Guangzhi XU and Xiaohui MA contribute to the development of the algorithms and data analyses. Guangzhi XU contributes to the writings of the manuscript, and all authors make significant contributions to its multiple revisions.

555   *Competing interests.* Neither I nor my co-authors have any competing interests involved.

Acknowledgements. This work is supported by the National Key Research and Development Program of China with grant NO. 2017YFC1404000. This work is also supported by the National Science Foundation of China (NSFC) with grant No. 41490644 (41490640). This is a collaborative project between the Ocean University of China (OUC), Texas A&M University (TAMU) and the National Center for Atmospheric Research (NCAR) and completed through the International Laboratory for High Resolution Earth System Prediction (iHESP)- a collaboration

560   by the Qingdao National Laboratory for Marine Science and Technology Development Center, Texas A&M University, and the National Center for Atmospheric Research. We also received support from the NSFC grant #41776013, and National Key Research and Development Program of China grant 2017YFC1404100 and 2017YFC1404101. We also give thanks to Chris Patricola from the Lawrence Berkeley National Laboratory, and Christine A. Shields from National Center for Atmospheric Research for their comments and suggestions to this manuscript.

565 References

Camargo, S. J. and Zebiak, S. E.: Improving the detection and tracking of tropical cyclones in atmospheric general circulation models, Weather and Forecasting, 17, 1152–1162, https://doi.org/10.1175/1520-0434(2002)017<1152:ITDATO>2.0.CO;2, 2002.

Dee, D. P., Uppala, S. M., Simmons, A. J., Berrisford, P., Poli, P., Kobayashi, S., Andrae, U., Balmaseda, M. A., Balsamo, G., Bauer, P., Bechtold, P., Beljaars, A. C. M., van de Berg, L., Bidlot, J., Bormann, N., Delsol, C., Dragani, R., Fuentes, M., Geer, A. J., Haimberger,
570 L., Healy, S. B., Hersbach, H., Hólm, E. V., Isaksen, L., KÅllberg, P. W., Köhler, M., Matricardi, M., McNally, A. P., Monge-Sanz, B. M., Morcrette, J. J., Park, B.-K., Peubey, C., de Rosnay, P., Tavolato, C., Thépaut, J. N., and Vitart, F.: The ERA-Interim reanalysis: configuration and performance of the data assimilation system, Quarterly Journal of the Royal Meteorological Society, 137, 553–597, https://doi.org/10.1002/qj.828, 2011.

Dettinger, M.: Climate Change, Atmospheric Rivers, and Floods in California – A Multimodel Analysis of Storm Frequency and
575 Magnitude Changes1, JAWRA Journal of the American Water Resources Association, 47, 514–523, https://doi.org/10.1111/j.1752-1688.2011.00546.x, 2011.

Dettinger, M. D.: Atmospheric Rivers as Drought Busters on the U.S. West Coast, Journal of Hydrometeorology, 14, 1721–1732, https://doi.org/10.1175/JHM-D-13-02.1, 2013.

Dijkstra, E. W.: A note on two problems in connexion with graphs, Numerische Mathematik, 1, 269–271,
580 https://doi.org/10.1007/BF01386390, 1959.

Dougherty, E.: Mathematical Morphology in Image Processing, Optical Science and Engineering, Taylor & Francis, 1992.

Dreyfus, G.: Neural Networks: Methodology and Applications, Springer Berlin Heidelberg, 2005.

Gimeno, L., Nieto, R., Vázquez, M., and Lavers, D. A.: Atmospheric rivers: a mini-review, Frontiers in Earth Science, 2, 1–6, https://doi.org/10.3389/feart.2014.00002, 2014.

585 Gorodetskaya, I. V., Tsukernik, M., Claes, K., Ralph, M. F., Neff, W. D., and Van Lipzig, N. P. M.: The role of atmospheric rivers in anomalous snow accumulation in East Antarctica, Geophysical Research Letters, 41, 6199–6206, https://doi.org/10.1002/2014GL060881, 2014.

Guan, B. and Waliser, D. E.: Detection of atmospheric rivers: Evaluation and application of an algorithm for global studies, Journal of Geophysical Research: Atmospheres, 120, 12 514–12 535, https://doi.org/10.1002/2015JD024257, 2015.

590 Guan, B. and Waliser, D. E.: Tracking Atmospheric Rivers Globally: Spatial Distributions and Temporal Evolution of Life Cycle Characteristics, Journal of Geophysical Research: Atmospheres, 124, 12 523–12 552, https://doi.org/10.1029/2019JD031205, 2019.

Hagos, S., Leung, L. R., Yang, Q., Zhao, C., and Lu, J.: Resolution and Dynamical Core Dependence of Atmospheric River Frequency in Global Model Simulations, Journal of Climate, 28, 2764–2776, https://doi.org/10.1175/JCLI-D-14-00567.1, 2015.

Hanley, J. and Caballero, R.: Objective identification and tracking of multicentre cyclones in the ERA-Interim reanalysis dataset, Quarterly
595 Journal of the Royal Meteorological Society, 138, 612–625, https://doi.org/10.1002/qj.948, 2012.

Hodges, K. I.: A General-Method For Tracking Analysis And Its Application To Meteorological Data, Monthly Weather Review, 122, 2573–2586, https://doi.org/10.1175/1520-0493(1994)122<2573:AGMFTA>2.0.CO;2, 1994.

Huttenlocher, D. P., Klanderman, G. A., and Rucklidge, W. J.: Comparing images using the Hausdorff distance, IEEE Transactions on Pattern Analysis and Machine Intelligence, 15, 850–863, 1993.

600 Kew, S. F., Sprenger, M., and Davies, H. C.: Potential Vorticity Anomalies of the Lowermost Stratosphere: A 10-Yr Winter Climatology, Monthly Weather Review, 138, 1234–1249, https://doi.org/10.1175/2009MWR3193.1, 2010.

Lavers, D. A. and Villarini, G.: Atmospheric Rivers and Flooding over the Central United States, Journal of Climate, 26, 7829–7836, https://doi.org/10.1175/JCLI-D-13-00212.1, 2013.

Lavers, D. A., Villarini, G., Allan, R. P., Wood, E. F., and Wade, A. J.: The detection of atmospheric rivers in atmospheric reanalyses and their links to British winter floods and the large-scale climatic circulation, Journal of Geophysical Research: Atmospheres, 117, https://doi.org/10.1029/2012JD018027, 2012.

Moore, B. J., Neiman, P. J., Ralph, F. M., and Barthold, F. E.: Physical Processes Associated with Heavy Flooding Rainfall in Nashville, Tennessee, and Vicinity during 1–2 May 2010: The Role of an Atmospheric River and Mesoscale Convective Systems, Monthly Weather Review, 140, 358–378, https://doi.org/10.1175/MWR-D-11-00126.1, 2012.

Mundhenk, B. D., Barnes, E. A., and Maloney, E. D.: All-Season Climatology and Variability of Atmospheric River Frequencies over the North Pacific, Journal of Climate, 29, 4885–4903, https://doi.org/10.1175/JCLI-D-15-0655.1, 2016.

Murakami, H., Vecchi, G. A., Underwood, S., Delworth, T. L., Wittenberg, A. T., Anderson, W. G., Chen, J. H., Gudgel, R. G., Harris, L. M., Lin, S. J., and Zeng, F.: Simulation and prediction of category 4 and 5 hurricanes in the high-resolution GFDL HiFLOR coupled climate model, Journal of Climate, 28, 9058–9079, https://doi.org/10.1175/JCLI-D-15-0216.1, 2015.

Nayak, M. A., Villarini, G., and Lavers, D. A.: On the skill of numerical weather prediction models to forecast atmospheric rivers over the central United States, Geophysical Research Letters, 41, 4354–4362, https://doi.org/10.1002/2014GL060299, 2014.

Neiman, P. J., Ralph, F. M., Wick, G. A., Lundquist, J. D., and Dettinger, M. D.: Meteorological Characteristics and Overland Precipitation Impacts of Atmospheric Rivers Affecting the West Coast of North America Based on Eight Years of SSM/I Satellite Observations, Journal of Hydrometeorology, 9, 22–47, https://doi.org/10.1175/2007JHM855.1, 2008.

Otsu, N.: A Threshold Selection Method from Gray-Level Histograms, IEEE Transactions on Systems, Man, and Cybernetics, 9, 62–66, https://doi.org/10.1109/TSMC.1979.4310076, 1979.

Ralph, F. M., Neiman, P. J., and Wick, G. A.: Satellite and CALJET Aircraft Observations of Atmospheric Rivers over the Eastern North Pacific Ocean during the Winter of 1997/98, Monthly Weather Review, 132, 1721–1745, https://doi.org/10.1175/1520-0493(2004)132<1721:SACAOO>2.0.CO;2, 2004.

Ralph, F. M., Wilson, A. M., Shulgina, T., Kawzenuk, B., Sellars, S., Rutz, J. J., Lamjiri, M. A., Barnes, E. A., Gershunov, A., Guan, B., Nardi, K. M., Osborne, T., and Wick, G. A.: ARTMIP-early start comparison of atmospheric river detection tools: how many atmospheric rivers hit northern California's Russian River watershed?, Climate Dynamics, 52, 4973–4994, https://doi.org/10.1007/s00382-018-4427-5, 2018.

Ralph, F. M., Rutz, J. J., Cordeira, J. M., Dettinger, M., Anderson, M., Reynolds, D., Schick, L. J., and Smallcomb, C.: A Scale to Characterize the Strength and Impacts of Atmospheric Rivers, Bulletin of the American Meteorological Society, 100, 269–289, https://doi.org/10.1175/bams-d-18-0023.1, 2019.

Rutz, J. J. and Steenburgh, W. J.: Quantifying the role of atmospheric rivers in the interior western United States, Atmospheric Science Letters, 13, 257–261, https://doi.org/10.1002/asl.392, 2012.

Rutz, J. J., Steenburgh, W. J., and Ralph, F. M.: Climatological Characteristics of Atmospheric Rivers and Their Inland Penetration over the Western United States, Monthly Weather Review, 142, 905–921, https://doi.org/10.1175/MWR-D-13-00168.1, 2014.

Rutz, J. J., Steenburgh, W. J., and Ralph, F. M.: The Inland Penetration of Atmospheric Rivers over Western North America: A Lagrangian Analysis, Monthly Weather Review, 143, 1924–1944, https://doi.org/10.1175/MWR-D-14-00288.1, 2015.

Sellars, S. L., Kawzenuk, B., Nguyen, P., Ralph, F. M., and Sorooshian, S.: Genesis, Pathways, and Terminations of Intense Global Water Vapor Transport in Association with Large-Scale Climate Patterns, Geophysical Research Letters, 44, 12,465–12,475, https://doi.org/10.1002/2017gl075495, 2017.

Shields, C. A., Rutz, J. J., Leung, L.-Y., Ralph, F. M., Wehner, M., Kawzenuk, B., Lora, J. M., McClenny, E., Osborne, T., Payne, A. E., Ullrich, P., Gershunov, A., Goldenson, N., Guan, B., Qian, Y., Ramos, A. M., Sarangi, C., Sellars, S., Gorodetskaya, I., Kashinath, K., Kurlin, V., Mahoney, K., Muszynski, G., Pierce, R., Subramanian, A. C., Tome, R., Waliser, D., Walton, D., Wick, G., Wilson, A., Lavers, D., Collow, A., Krishnan, H., Magnusdottir, G., and Nguyen, P.: Atmospheric River Tracking Method Intercomparison Project (ARTMIP): project goals and experimental design, Geoscientific Model Development, 11, 2455–2474, https://doi.org/10.5194/gmd-11-2455-2018, 2018.

van der Walt, S., Schönberger, J. L., Nunez-Iglesias, J., Boulogne, F., Warner, J. D., Yager, N., Gouillart, E., Yu, T., and the scikit-image contributors: scikit-image: image processing in Python, PeerJ, 2, e453, https://doi.org/10.7717/peerj.453, 2014.

Vergeest, J., Spanjaard, S., and Song, Y.: Directed mean Hausdorff distance of parameterized freeform shapes in 3D: a case study, The Visual Computer, 19, 480–492, https://doi.org/10.1007/s00371-003-0213-3, 2003.

Vincent, L.: Morphological grayscale reconstruction in image analysis: applications and efficient algorithms, IEEE Transactions on Image Processing, 2, 176–201, https://doi.org/10.1109/83.217222, 1993.

Wernli, H.: A lagrangian-based analysis of extratropical cyclones. II: A detailed case-study, Quarterly Journal of the Royal Meteorological Society, 123, 1677–1706, https://doi.org/10.1002/qj.49712354211, 1997.

Wick, G. A., Neiman, P. J., and Ralph, F. M.: Description and Validation of an Automated Objective Technique for Identification and Characterization of the Integrated Water Vapor Signature of Atmospheric Rivers, IEEE Transactions on Geoscience and Remote Sensing, 51, 2166–2176, https://doi.org/10.1109/TGRS.2012.2211024, 2013.

XU, G., MA, X., CHANG, P., and WANG, L.: Image-Processing based Atmospheric River Tracking (IPART) algorithms version 1, Zenodo, https://doi.org/10.5281/zenodo.3864592, 2020.

Zhou, Y., Kim, H., and Guan, B.: Life Cycle of Atmospheric Rivers: Identification and Climatological Characteristics, Journal of Geophysical Research: Atmospheres, 123, 12,715–12,725, https://doi.org/10.1029/2018JD029180, 2018.